$\underline{\bullet}$

Click here to view linked References

inviscid and viscous conical nozzle flows

Verification and validation of high-resolution

Luciano K. Araki¹, Rafael B. de R. Borges², Nicholas Dicati P. da Silva^{3*} and Chi-Wang Shu⁴

¹Department of Mechanical Engineering, Federal University of Paraná, Curitiba, 81531-980, Paraná, Brasil. ²Mathematics and Statistics Institute, Rio de Janeiro State

University, Rio de Janeiro, 20550-900, Rio de Janeiro, Brasil. ^{3*}Department of Mechanical Engineering, State University of

Maringá, Maringá, 87020-900, Paraná, Brasil. ⁴Division of Applied Mathematics, Brown University, Providence,

02912, Rhode Island, USA.

*Corresponding author(s). E-mail(s): ndicati@gmail.com; Contributing authors: lucaraki@ufpr.br; rafael.borges@ime.ueri.br; chi-wang_shu@brown.edu;

Abstract

Capturing elaborated flow structures and phenomena is required for well-solved numerical flows. The finite difference methods allow simple discretization of mesh and model equations. However, they need simpler meshes, e.g., rectangular. The inverse Lax-Wendroff (ILW) procedure can handle complex geometries for rectangular meshes. High-resolution and high-order methods can capture elaborated flow structures and phenomena. They also have strong mathematical and physical backgrounds, such as positivity-preserving, jump conditions, and wave propagation concepts. We perceive an effort toward direct numerical simulation, for instance, regarding weighted essentially non-oscillatory (WENO) schemes. Thus, we propose to solve a challenging engineering application without turbulence models. We aim to verify and validate recent high-resolution and high-order methods. To check the solver accuracy, we solved vortex and Couette flows. Then, we solved inviscid and viscous nozzle flows for a conical profile. We employed the finite difference method, positivity-preserving Lax-Friedrichs splitting, high-resolution

10 11

12 13

14

15

16

17

18

19 20

21

26 27

28

29

30

31

32 33

34

35

36

37

38

39

40

41

42

43

44

45

46

47

48

49 50

51

52

53

54

55

56

57

58

59

2 Verification and validation of high-resolution inviscid and viscous conical nozzle flows

viscous terms discretization, fifth-order multi-resolution WENO, ILW, and third-order strong stability preserving Runge-Kutta. We showed the solver is high-order and captured elaborated flow structures and phenomena. One can see oblique shocks in both nozzle flows. In the viscous flow, we also captured a free-shock separation, recirculation, entrainment region, Mach disk, and the diamond-shaped pattern of nozzle flows.

Keywords: high-resolution, compressible, Navier-Stokes, free-shock separation, nozzle flow

1 Introduction

The nozzle flow is a challenging engineering, experimental, and numerical application. One can study the nozzle flow in various ways, and rocket science is one of the most popular. Due to the nature of the flow and phenomena, one needs to solve a system of nonlinear partial differential equations. One could simplify the model and obtain exact quasi-one-dimensional solutions [1]. However, this would limit the number of captured phenomena.

Capturing elaborated flow phenomena requires particle image velocimetry or other advanced experimental techniques. Still, not every flow can be captured. The experiment requires robust sensors and well-fabricated nozzles, and the most common approach is to measure the wall pressure distribution [2–6]. Detailed descriptions of the nozzle contour and experimental data are not easily found. A classical paper by Back et al. [7] presents the nozzle contour for a conical profile and experimental data for hot gas flows.

High-resolution and high-order methods had a fast growth in the past decades, mostly because of their capability of capturing elaborated phenomena [8, 9]. Those schemes can have physical and mathematical concepts in their formulations [8, 10]. Recent weighted essentially non-oscillatory schemes (WENO) can maintain symmetry and reach machine error for residual in steady-state computation [8, 11].

The finite difference scheme is well known for its simple discretization techniques. One does not need strategies for maintaining the order of the numerical approximations. As a result, structured meshes are needed [12]. The recent developments in the inverse Lax-Wendroff (ILW) boundary treatment allow the computation of complex geometries for computational fluid dynamics problems [9, 13-15].

It is still possible to find a lack of agreement between numerical and experimental data for elaborated flows, e.g., in turbine blade cascade flows [16, 17]. For instance, to adequately capture side loads, one needs to solve the transient 3D Navier-Stokes equations [18]. Recently, we can see efforts toward direct numerical simulations [19]. However, the hardware requirements are still restraining.

Verification and validation of high-resolution inviscid and viscous conical nozzle flows

The objective of this work is to test recent high-resolution and highorder methods in solving convergent-divergent conical nozzle flows. We also discussed modeling strategies, mesh construction, and boundary conditions. To reach the objective, we employed the finite difference method [12] with the positivity-preserving Lax-Friedrichs splitting [10], high-resolution viscous terms discretization [15], fifth-order multi-resolution WENO [8], ILW [9, 13– 15, 20, and the third-order strong stability preserving Runge–Kutta [12]. The remaining text is organized as follows, the governing equations and numerical methods are presented in Sec. 2. We discussed the inviscid fluid model in Sec. 3, disclosed the viscous fluid model in Sec. 4, and presented concluding remarks in Sec. 5.

Governing Equations and Numerical Methods

We are interested in inviscid and viscous flows described by the Euler $(S_1 = S_2 = S_{NS} = 0)$ and Navier-Stokes equations

$$U_t + F(U)_x + G(U)_y = S_{1x} + S_{2y} + S_E + S_{NS},$$
 (1)

with

$$U = \begin{bmatrix} \rho \\ \rho u \\ \rho v \\ E \end{bmatrix}, \quad F(U) = \begin{bmatrix} \rho u \\ \rho u^2 + p \\ \rho u v \\ u(E+p) \end{bmatrix}, \quad G(U) = \begin{bmatrix} \rho v \\ \rho u v \\ \rho v^2 + p \\ v(E+p) \end{bmatrix}, \quad (2)$$

$$\boldsymbol{S}_{1} = \begin{bmatrix} 0 \\ \tau_{xx} \\ \tau_{xy} \\ u\tau_{xx} + v\tau_{xy} + \frac{\mu}{Pr(\gamma-1)} \frac{\partial(a^{2})}{\partial x} \end{bmatrix}, \quad \boldsymbol{S}_{2} = \begin{bmatrix} 0 \\ \tau_{xy} \\ \tau_{yy} \\ u\tau_{xy} + v\tau_{yy} + \frac{\mu}{Pr(\gamma-1)} \frac{\partial(a^{2})}{\partial y} \end{bmatrix},$$

$$E = \frac{p}{\gamma - 1} + \frac{\rho}{2}(u^2 + v^2), \ \tau_{xx} = \mu \left(\frac{4}{3}\frac{\partial u}{\partial x} - \frac{2}{3}\frac{\partial v}{\partial y}\right),\tag{4}$$

$$\tau_{xy} = \mu \left(\frac{\partial u}{\partial y} + \frac{\partial v}{\partial x} \right), \ \tau_{yy} = \mu \left(\frac{4}{3} \frac{\partial v}{\partial y} - \frac{2}{3} \frac{\partial u}{\partial x} \right), \tag{5}$$

$$\boldsymbol{S}_{E} = -\frac{1}{y} \begin{bmatrix} \rho v \\ \rho u v \\ \rho v^{2} \\ v(E+p) \end{bmatrix}, \quad \boldsymbol{S}_{NS} = \frac{1}{y} \begin{bmatrix} 0 \\ \tau_{xy} \\ -\frac{4v\mu}{3y} + 2\mu\frac{\partial v}{\partial y} \\ u\tau_{xy} + v\tau_{yy} + \frac{\mu}{Pr(\gamma-1)}\frac{\partial(a^{2})}{\partial y} \end{bmatrix}, \quad (6)$$

where ρ is the density, u and v are the x- and y-direction velocities, p is the pressure, E is the energy per unit volume, $a = \sqrt{\gamma p/\rho}$ is the speed of sound, μ is the absolute viscosity, and Pr is the Prandtl number. S_E and S_{NS} are the source terms for axisymmetric cylindrical coordinates flow.

Verification and validation of high-resolution inviscid and viscous conical nozzle flows

We discretize the model equations with a conservative scheme [21]

$$\frac{d\mathbf{U}_{i,j}}{dt} = -\frac{1}{\Delta x} \left(\hat{\mathbf{F}}_{i+1/2,j} - \hat{\mathbf{F}}_{i-1/2,j} \right) - \frac{1}{\Delta y} \left(\hat{\mathbf{G}}_{i,j+1/2} - \hat{\mathbf{G}}_{i,j-1/2} \right) + (\mathbf{S}_{1x})_{i,j} + (\mathbf{S}_{2y})_{i,j} + (\mathbf{S}_{E})_{i,j} + (\mathbf{S}_{NS})_{i,j},$$
(7)

and apply the positivity-preserving Lax–Friedrichs splitting flux and high-resolution viscous terms discretization [10, 15].

The numerical fluxes for the splitting are approximated with the multiresolution WENO [8]. To finish the spatial approximation, we use the ILW procedure to apply the boundary conditions [9, 14, 15]. Then, we integrate in time with the strong stability preserving Runge-Kutta [12].

3 Inviscid Nozzle Flow

3.1 Vortex flow accuracy check

Testing the accuracy of a nozzle flow is a difficult task. For adiabatic and inviscid flows, the total temperature is constant, and we could use it to verify the accuracy [1]. However, one has to design the nozzle profile to avoid shock waves because shocks prevent the observed accuracy from reaching the designed order [22, 23]. One can obtain the optimal nozzle profile through different methods [1, 24–26]. For instance, Anderson [1] presents a strategy based on characteristic lines. For illustration purposes, we show the optimal profile for the method of [1] and a cosinoidal function in Fig. 1.

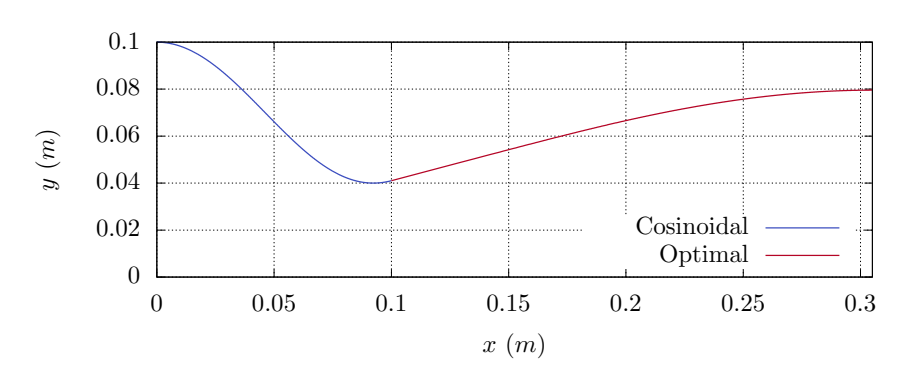


Fig. 1 Optimal nozzle profile for a cosinoidal function.

As stated in [1], the method has drawbacks, e.g., the sonic line is considered straight, and the Mach number, M, is one at the nozzle throat for a preliminary analysis. That does not agree with theoretical or experimental data [7, 27]. The author suggests that the method can be improved with finite

12 13

14 15

16

17

18

19 20

21

22

23

24

25

26

27

28

29

30

31

32 33

34

35 36

37 38 39

40

41

42

43

44

45

46

47

48

49 50

51

52

53

54

55

56

57

58

59

60

difference techniques. In addition, the optimal nozzle profile will be a collection of points and inclinations connected through straight lines. For applying the wall boundary treatment, Tan et al. [20] suggest that

Verification and validation of high-resolution inviscid and viscous conical nozzle flows

$$p_{\hat{x}} = -\rho \hat{v}^2 \kappa, \tag{8}$$

where \hat{x} is the normal direction, \hat{v} is the velocity in the tangential direction, \hat{y} , and κ is the curvature.

We need the second derivative to compute the curvature and a strategy to compute the former. Also, the straight lines profile can cause problems with the high-order methods [21]. Fitting a polynomial function for the optimal nozzle profile can also be a difficult task. For instance, the maximum inclination angle of the nozzle wall can increase. A new maximum inclination requires a new optimal profile.

One can tackle the mentioned drawbacks or choose another method to obtain the optimal nozzle profile. Since our goal is to perform an accuracy test, we propose to solve a vortex flow [12, 15]. It has similarities to the nozzle flow and is enough to test the numerical methods.

Consider a flow with $\rho = p = 1$ and v = u = 0. We add perturbations to it in u, v, and $T = p/\rho$

$$(\delta u, \delta v) = \frac{\epsilon}{2\pi} \exp\left[0.5(1-r^2)\right] (y, -x), \ \delta T = -\frac{(\gamma - 1)\epsilon^2}{8\gamma \pi^2} \exp\left(1 - r^2\right), \ \delta s = 0,$$

where $r^2 = x^2 + y^2$, R = 1, $\gamma = 1.4$, the vortex strength is $\epsilon = 5$, and $s = p/\rho^{\gamma}$ is the entropy.

We use the perturbed solution as the exact solution. The computational domain is bounded by x = 0 and y = 0 lines and a circular arc with a radius of two. The normal velocity is zero in the arc boundary, and we employ the ILW for solid walls. The left boundary is an inflow computed with total properties. We determined the lower ghost points with the exact solution.

For the Euler equations and at the wall, we need one boundary condition if imposing in the normal direction [14]. However, if no rotation is performed, up to three boundary conditions may be required [15, 21]. Since we only know the normal velocity, $\hat{u} = 0$, and the heat flux, we may lack one boundary condition. For the Navier–Stokes equations, we also have $\hat{v} = 0$, which solves the lack of boundary conditions at the wall. Therefore we will rotate and apply the wall boundary conditions in the normal direction for Euler only.

Suppose we want to impose the boundary conditions at the point (x_0, y_0) in Fig. 2. We select the nearest $a(r+1)^2$ points to construct two-dimensional least squares polynomials of r-th degree, shown as crosses for r = 4. If not stable, we use a > 1 for improving the least squares approximation. Otherwise, we use a=1. We remark that the least squares strategy is flexible, if one maintains the order and the approximation is stable. The WENO-type extrapolation stencil S_4 is denoted by circles. As stated in [9], better results

for high-magnitude variables can be achieved by using the characteristic variables, V. We rotate the nearest points and compute the characteristic variables to construct the polynomials. The stencil S_0 is set with the nearest point to (x_0, y_0) . The stencil S_1 is computed with a first-degree least squares polynomial. The remaining stencils are computed similarly. For completeness, the rotation matrix is

$$T = \begin{pmatrix} \cos(\theta) & \sin(\theta) \\ -\sin(\theta) & \cos(\theta) \end{pmatrix}. \tag{10}$$

Verification and validation of high-resolution inviscid and viscous conical nozzle flows

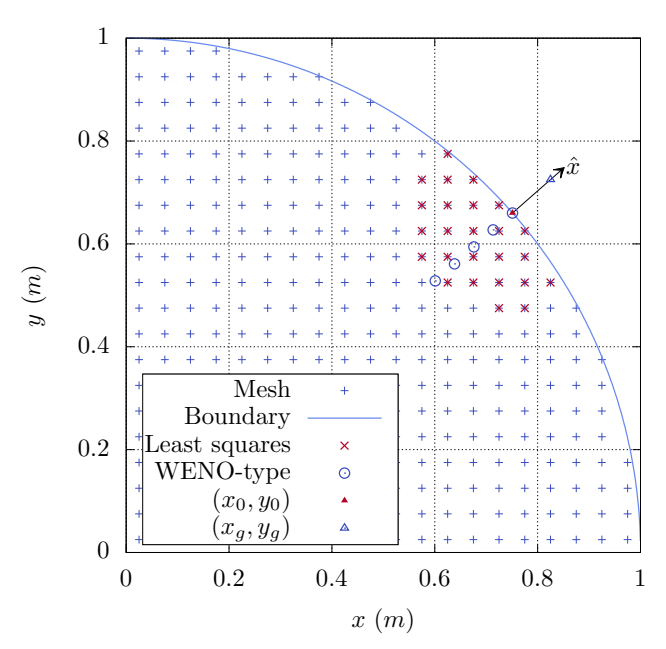


Fig. 2 Vortex flow mesh, boundary, stencils, and ghost point.

Now, we use the WENO-type extrapolation of [9] to obtain $\{\partial_{\hat{x}}^{(l)}\hat{V}\}_{l=0}^{l=4}$ at (x_0,y_0) . For the vortex problem, we have $\hat{\lambda}_1<0$, $\hat{\lambda}_m\approx 0$ for m=2,3, and $\hat{\lambda}_4 > 0$. Since we also know the heat flux or the temperature derivative, we compute the temperature in the stencils shifted to the interior of the domain. That is, the point (x_0, y_0) is not used. As in [15], we use a similar strategy for the WENO-type extrapolation and a known temperature derivative to obtain the temperature at (x_0, y_0) . Knowing $\hat{U}_2 = 0, T$, and T_0 , we solve the following system

$$R\left(T - \frac{\gamma T_0}{\gamma - 1}\right) \hat{U}_1 + \hat{U}_4 = 0,$$

$$\hat{l}_{3,1} \hat{U}_1 + \hat{l}_{3,3} \hat{U}_3 + \hat{l}_{3,4} \hat{U}_1 = \partial_{\hat{x}}^{(0)} \hat{V}_3,$$

$$\hat{l}_{4,1} \hat{U}_1 + \hat{l}_{4,3} \hat{U}_3 + \hat{l}_{4,4} \hat{U}_1 = \partial_{\hat{x}}^{(0)} \hat{V}_4,$$
(11)

(12)

(13)

temperature derivative. Thus, we compute

can approximate

 $oldsymbol{W} = \left| egin{array}{c}
ho \ Ma\cos heta_V \ Ma\sin heta_V \end{array}
ight| \, .$ (18)

With \boldsymbol{W} we can compute \boldsymbol{U} and update

 $\partial_{-}^{(0)}V_k = \boldsymbol{l}_k \cdot \boldsymbol{U}, \quad k = 2, 3, 4.$ (19)

$$(\hat{U}_1)_{\hat{x}} = \frac{\hat{p}_{\hat{x}}}{PT} - \frac{\hat{p}\hat{T}_{\hat{x}}}{PT^2},\tag{13}$$

$$\partial_{\hat{x}}^{(1)} \hat{V}_{1} = \frac{(\hat{U}_{1})_{\hat{x}} - \hat{r}_{1,2} \partial_{\hat{x}}^{(1)} \hat{V}_{2} - \hat{r}_{1,3} \partial_{\hat{x}}^{(1)} \hat{V}_{3} - \hat{r}_{1,4} \partial_{\hat{x}}^{(1)} \hat{V}_{4}}{\hat{r}_{1,1}} \tag{14}$$

Verification and validation of high-resolution inviscid and viscous conical nozzle flows

where \hat{L} is the rotated left eigenvectors matrix, \hat{U} are the rotated U, and the

first equation comes from the total enthalpy $H = (E + p)/\rho$. Then, we update

 $\partial_{\hat{a}}^{(0)}\hat{V}_1 = \hat{\boldsymbol{l}}_1 \cdot \hat{\boldsymbol{U}}, \quad \partial_{\hat{a}}^{(0)}\hat{V}_2 = \hat{\boldsymbol{l}}_2 \cdot \hat{\boldsymbol{U}}.$

For the first derivative, we know the pressure derivative from (8) and the

Now, we use a Taylor expansion to approximate the characteristic variables at the ghost point (x_q, y_q) ,

$$\hat{\mathbf{V}}_{x_g,y_g} = \sum_{l=1}^{l=4} \frac{\Delta^l}{l!} \partial_{\hat{x}}^{(l)} \hat{\mathbf{V}}, \tag{15}$$

where Δ is the distance between (x_0, y_0) and (x_q, y_q) after the rotation.

Finally, we transform to the conservative variables and rotate back. At the left boundary, we want to mimic the nozzle inflow. In which we have the total properties. Unfortunately, the gas dynamics relations are nonlinear equations to the flow variables [1]

One could use the interior points and solve a nonlinear system. However,

this can easily increase the computational cost and cause instability. We pro-

pose to compute the Mach number and the flow direction, θ_V , at the boundary

using the characteristic variables and WENO-type extrapolation. Then, we

$$\frac{T_0}{T} = 1 + \frac{(\gamma - 1)}{2} M^2,\tag{16}$$

$$\frac{p_0}{n} = \left[1 + \frac{(\gamma - 1)}{2} M^2 \right]^{\gamma/(\gamma - 1)}.$$
 (17)

For the first derivative, we consider v_x and H_x as known. Therefore, we can use the Euler equation and the known information to form the system

$$\rho_x H + \rho H_x = \frac{p_x}{\gamma - 1} + \frac{\rho_x}{2} (u^2 + v^2) + \rho (uu_x + vv_x) + p_x,$$

$$p_x = -\rho (uu_x + vv_x),$$

$$l'_{1,1} \rho_x + l'_{1,2} u_x + l'_{1,3} v_x + l'_{1,4} p_x = \partial_x^{(1)} V_1,$$
(20)

Verification and validation of high-resolution inviscid and viscous conical nozzle flows

where $\boldsymbol{L}' = \boldsymbol{L} \partial \boldsymbol{U} / \partial \boldsymbol{W}$ and

$$\frac{\partial \mathbf{U}}{\partial \mathbf{W}} = \begin{bmatrix} 1 & 0 & 0 & 0 \\ u & \rho & 0 & 0 \\ v & 0 & \rho & 0 \\ \frac{(u^2 + v^2)}{2} & \rho u & \rho v & \frac{1}{1 - 1} \end{bmatrix}. \tag{21}$$

The accuracy results are shown in Tab. 1, were we can see that high order was reached.

Table 1 Accuracy results for the vortex flow.

$\Delta x = \Delta y$	L^1		L^2		L^{∞}	
	\mathbf{Norm}	\mathbf{Order}	\mathbf{Norm}	\mathbf{Order}	\mathbf{Norm}	Order
2/10	3.91E-04	-	5.09E-04	-	1.53E-03	-
2/20	2.84E-05	3.78	4.01E-05	3.67	1.73E-04	3.15
2/40	1.56E-06	4.19	2.78E-06	3.85	1.76E-05	3.30
2/80	9.37E-08	4.06	1.78E-07	3.96	1.20E-06	3.88
2/160	5.86E-09	4.00	1.14E-08	3.97	7.96E-08	3.91

3.2 Verification and validation

We now have the core solver for the Euler equations and most of the boundary treatment verified. For axisymmetric flows, the lower boundary can be set as the symmetry line. This type of boundary condition is easy to impose. For Euler flows, the nozzle exit will be supersonic, and we can extrapolate all characteristic variables. Depending on the mesh size and discretization, one may not have enough points to construct the WENO-type extrapolation stencils. In this case, the 2D least squares polynomials can provide the remaining points.

The nozzle flow can be considered as adiabatic [7] and irrotational, i.e., H = constant and $v_x = u_y$. The y-derivative is approximated with characteristic variables, least squares, and WENO-type extrapolation, see e.g. [9, 14, 15]. Then, we use this information in the vortex flow left boundary strategy. At the wall, $\hat{u} = 0$ and $T_{\hat{x}} = 0$. Therefore, we use the same strategy as for the vortex flow arc boundary.

We solve a nozzle flow for the $45^{\circ} - 15^{\circ}$ conical profile of [7] with $p_0 \approx 1.725 \ MPa$, $T_0 = 833.\overline{3} \ K$, and $r_{th} = 20.32 \ mm$. The other flow properties are computed with the CoolProp library [28] and total properties. The

Verification and validation of high-resolution inviscid and viscous conical nozzle flows

resulting flow has an oblique shock, which prevents an accuracy analysis [21–23]. We use the total temperature of the chamber as a reference and compute the absolute difference with the point-wise total temperature. One can see in Fig. 3 that the total temperature is constant in certain regions of the flow for the $\Delta_x = r_{th}/80$ mesh. The shock region gives rise to numerical errors and increases the difference between total temperatures. We remark that inflow, wall, and symmetry line boundaries do not change the total temperature.

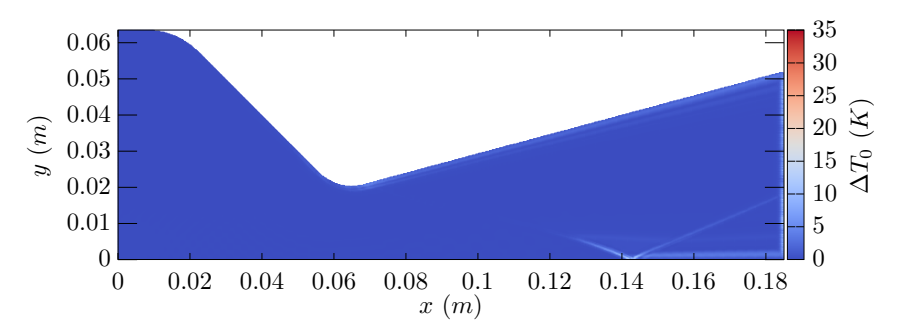


Fig. 3 Absolute difference of the total temperature for the inviscid flow and the $\Delta_x = r_{th}/80$ mesh.

The Euler equations are well established as a model to study nozzle flows [29]. However, numerical approximations such as flux splitting, schemes, and boundary treatment may also have physical approximations. Therefore, it is interesting to present a validation. We show the wall pressure for the $\Delta x = r_{th}/80$ mesh, quasi-one-dimensional exact solution, and experimental data of [7] in Fig. 4. One can see that the numerical solution is close to the experimental data. Since the data were digitized, we present a simple comparison and proceed no further.

We remark that after x=0.12 m, the pressure is lower than the atmospheric. This happens because we imposed a supersonic outflow boundary treatment. That is, the flow will continue to expand. We also show the Mach number color map in Fig. 5 for the $\Delta x = r_{th}/80$ mesh, where one should notice the shock position and flow behavior near the exit and wall.

4 Viscous Nozzle Flow

4.1 Couette flow accuracy check

Obtaining smooth analytical or exact solutions for 2D Euler nozzle flows is not a simple task, and it does not get any better for Navier–Stokes equations. Therefore, we propose to verify the solver and wall boundary treatment accuracies with a Couette flow. We could proceed as in [15], but the pressure high magnitude can cause problems. Therefore, we propose to use the characteristic

Verification and validation of high-resolution inviscid and viscous conical nozzle flow

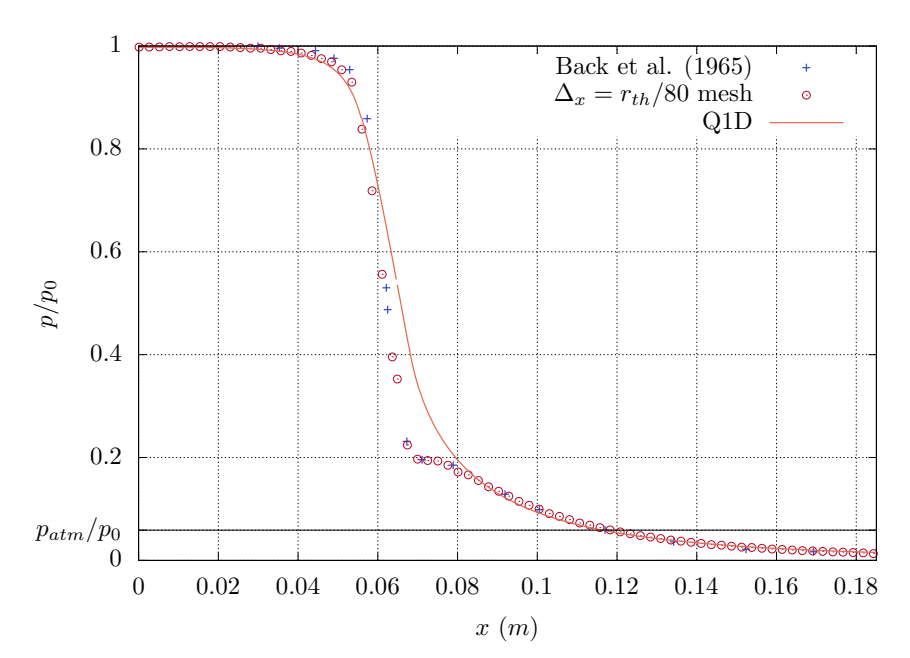


Fig. 4 Nozzle wall pressures for the inviscid flow and $\Delta_x = r_{th}/80$ mesh.

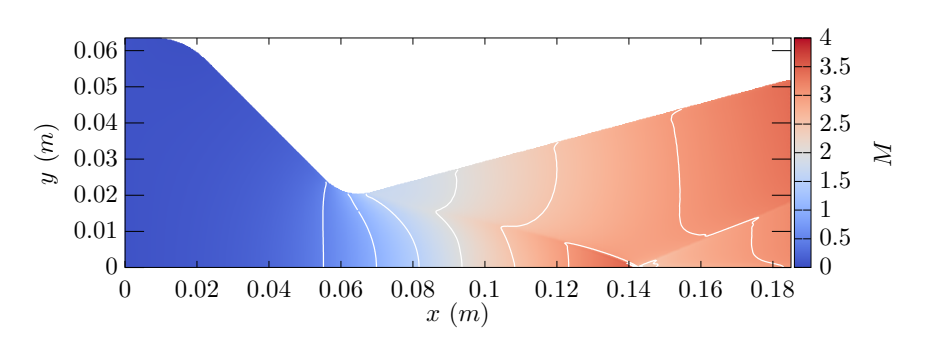


Fig. 5 Mach number color map for the inviscid flow and $\Delta_x = r_{th}/80$ mesh.

variable approach as in [9]. We set the domain as $[0, 20] \times [0, 10]$ and compute the analytical solution as in [15]. We use the analytical solution in the lower, left, and right ghost points. The upper boundary is a moving wall where we apply the ILW as presented next.

We chose the upper wall boundary to explain the strategy, which is analogous to the left and right nozzle wall boundaries. Suppose we want to compute the boundary conditions at the wall, (x_0, y_0) . We know u_{wall} , v_{wall} , and $T_{\hat{x}}$. We compute the temperature in normal stencils to the boundary and approximate it at (x_0, y_0) with a WENO-type extrapolation for a known temperature derivative. The characteristic variables are computed in y-direction stencils.

Then, we have [9, 15]

$$\boldsymbol{W} = \begin{bmatrix} \frac{\partial_{y}^{(0)} V_{4}}{l_{4,1} + u_{\text{wall}} l_{4,2} + v_{\text{wall}} l_{4,3} + l_{4,4} \left(\frac{RT_{\text{wall}}}{\gamma - 1} + \frac{u_{\text{wall}}^{2} + v_{\text{wall}}^{2}}{2}\right)}{u_{\text{wall}}} \\ v_{\text{wall}} \\ V_{1}RT_{\text{wall}} \end{bmatrix}.$$
(22)

Verification and validation of high-resolution inviscid and viscous conical nozzle flows

With W, we compute U and update $\partial_y^{(0)}(V_{ccc})_m = l_m U$ for m = 2, 3, 4, where the subscript *ccc* represents the convective part for the convex combination. For the first derivative, we compute [9, 14, 15]

$$\partial_{y}^{(1)}(V_{ccc})_{1} = \frac{(S_{E})_{1} + (S_{NS})_{1} - (F_{1})_{x} - r_{1,2}v_{\text{wall}}\partial_{y}^{(1)}(V_{ccc})_{2}}{r_{1,1}(v_{\text{wall}} - a)} + \frac{-r_{1,3}v_{\text{wall}}\partial_{y}^{(1)}(V_{ccc})_{3} - r_{1,4}(v_{\text{wall}} + a)\partial_{y}^{(1)}(V_{ccc})_{4}}{r_{1,1}(v_{\text{wall}} - a)}.$$
(23)

For the diffusive part, [9, 13–15]

$$W = \begin{bmatrix} \frac{\partial_{y}^{(0)}(V_{d})_{4}}{(l_{d})_{4,1} + u_{\text{wall}}(l_{d})_{4,2} + v_{\text{wall}}l_{4,3} + (l_{d})_{4,4} \left(\frac{RT_{\text{wall}}}{\gamma - 1} + \frac{u_{\text{wall}}^{2} + v_{\text{wall}}^{2}}{2}\right)}{u_{\text{wall}}} \\ v_{\text{wall}} \\ W_{1}RT_{\text{wall}} \end{bmatrix}.$$
(24)

With W, we compute U and update $\partial_y^{(0)}(V_d)_m = (l_d)_m U$ for m = 2, 3, 4. For the second derivative, we have [9, 13-15]

$$\mathbf{l}_{d4}\mathbf{U}_{yy} = \partial_y^{(2)}(V_d)_4,
\Psi_{1m}(U_m)_{yy} = (U_m)_t + F_m(\mathbf{U})_x + G_m(\mathbf{U})_y -
\Psi_{1m}\mathbf{U}_{xx} - \Psi_{3m}\mathbf{U}_{xy} - N_m, m = 2, 3, 4.$$
(25)

Then, we update $\partial_y^{(2)}(V_d)_m = (\boldsymbol{l}_d)_m \boldsymbol{U}_{yy}$ for m = 2, 3, 4. We compute

$$\{\partial_{\nu}^{(l)} \boldsymbol{V}_{ccd}\}_{l=0}^{4} = \boldsymbol{L} \boldsymbol{R}_{d} \{\partial_{\nu}^{(l)} \boldsymbol{V}_{d}\}_{l=0}^{4}, \tag{26}$$

and perform the convex combination [9]

$$\{\partial_{y}^{(l)}V\}_{l=0}^{4} = \alpha \{\partial_{y}^{(l)}V_{ccc}\}_{l=0}^{4} + (1-\alpha)\{\partial_{y}^{(l)}V_{ccd}\}_{l=0}^{4}, \tag{27}$$

where α is obtained by decomposing and rearranging (1).

Now, we use a Taylor expansion to compute the characteristic variables and their derivatives at the ghost point and then $U, W, W_x, W_y, G(U)$, and

 S_2 . For simplicity and to avoid a cumbersome description, we refer to [9, 13-15] for formulae and further details. The accuracy results are shown in Tab. 2, where we can see that it is high order.

Verification and validation of high-resolution inviscid and viscous conical nozzle flow

Table 2 Accuracy results for the Couette flow.

$\Delta x = \Delta y$	L^1		L^2		L^{∞}	
	\mathbf{Norm}	\mathbf{Order}	\mathbf{Norm}	\mathbf{Order}	\mathbf{Norm}	\mathbf{Order}
10/10	4.37E-07	-	5.12E-07	-	1.36E-06	_
10/20	1.25E-08	5.13	1.54E-08	5.05	4.32E-08	4.98
10/40	3.91E-10	5.00	5.00E-10	4.95	1.60E-09	4.76
10/80	1.22E-11	5.01	1.62E-11	4.95	6.62E-11	4.59
10/160	7.81E-14	7.28	2.58E-13	5.97	2.73E-12	4.60

4.2 Domain design

For simplicity, we use the same inflow strategy as the inviscid nozzle flow, i.e., an isentropic and irrotational inflow. This is a hard-to-obtain idealized experimental setup for nozzle inflows, even for hot gas flows. In real rocket nozzle applications, the flow will have various chemical components and will not be irrotational because of the viscosity. However, the inviscid inflow is an easy-to-impose boundary treatment and a suitable approximation for hot gas flows. In addition to the strategy for the inviscid flow, we compute the diffusive terms and perform a convex combination.

For the viscous flow, the no-slip approximation will cause the flow to be subsonic near the nozzle wall. Without the appropriate boundary conditions, we cannot impose the outflow for the same domain as the inviscid nozzle flow. As stated in [9], we must respect the speed regime and phenomena to impose the ILW outflow accurately. This could be solved by, e.g., experimental data or extending the domain.

We first tried to shortly extend the computational domain and use the ILW outflow boundary treatment with atmospheric conditions. However, neither U nor the total properties are constant for a y line at the nozzle discharge. The right boundary for this case can have mixed flow regimes: subsonic and supersonic outflow and subsonic inflow. We tried to enforce an outflow only. Despite our efforts, a strong recirculation appeared near the right boundary, which is not physical because it does not happen in larger domains.

Highly extending the domain is a non-efficient way to simulate atmospheric conditions. For a high-order and high-resolution solver, this will highly limit the mesh size, depending on the available hardware. We also tried extending the domain 5 times the nozzle length in the x-direction and 15 times the nozzle exit radius in the r-direction. This is not a large domain since it can be larger than a hundred times the nozzle throat [4, 6].

We started the flow in a coarse mesh with u = v = 0 everywhere and a linear variation from W_0 at the inflow and W_{atm} at the nozzle throat. A high-speed flow rapidly develops after a few steps. When the high-speed flow reaches the

extended domain, waves and disturbances are generated. As long as the waves and disturbances are sufficiently far, do not interact with the boundaries, and reflect, the flow near the nozzle will be approximated as undisturbed. In other words, the nozzle flow will behave as discharging to the atmosphere.

For the Navier–Stokes equations, the initial estimate plays an important role. It can cause the solution to blow up. For example, a supersonic flow near the nozzle wall can cause high expanse or compression, generating strong waves. In turn, these waves can cause problems at the high-order and high-resolution boundaries. To soften this issue, we use as the initial guess the coarse mesh solution with the characteristic boundary everywhere [9].

Differently from the Euler equations, we cannot assume that total temperature is constant, as it can rise because of friction and atmospheric condition. Furthermore, disturbances can propagate in the low-speed region of the domain and affect the plume. These disturbances are not necessarily physical, as they could result from numerical errors as the solution is adjusting to the new mesh or new phenomena are being captured. Therefore, we conclude that good approximations for the outflow would require fine mesh solutions in large domains.

Imposing constant subsonic or supersonic speeds with total properties can cause overexpansion or the flow to change direction, as would happen in the presence of disturbances. The latter can lead to nonrealistic vortices and the former to a nonphysical vacuum and cause the solution to blow up [9]. We remark that this happens in the boundary treatment and ghost points since the interior scheme has the positivity-preserving property.

To solve the lack of information, one could gather experimental data at suitable locations. Numerically, we are left with the non-efficient boundary extension. To lower the hardware requirements, we propose to use the Navier–Stokes equations in the nozzle and a short domain extension, high-order Navier–Stokes and Euler equations in two small transitions, and lower-order Euler equations in the remaining meshes with increasing mesh sizes. The sixth mesh size is twice big as the fifth, and so on. The mesh configuration is shown in Fig. 6. To summarize, the model, mesh size, scheme accuracy, and boundary treatment for each mesh are

- 1-2. Navier–Stokes, fine, fifth order, and ILW inflow and wall boundary treatments:
 - 3. Navier–Stokes, fine, fifth order, and ILW inflow boundary treatment;
 - 4. Navier–Stokes, fine, fifth order, and characteristic boundary;
 - 5. Euler, fine, fifth order, and characteristic boundary;
- 6-9. Euler, increasing mesh sizes, first order, and characteristic boundary.

4.3 Verification and validation

Particularly for this case, the supersonic flow near the boundary layer can cause trouble with the wall boundary treatment. We, therefore, changed the

Verification and validation of high-resolution inviscid and viscous conical nozzle flow

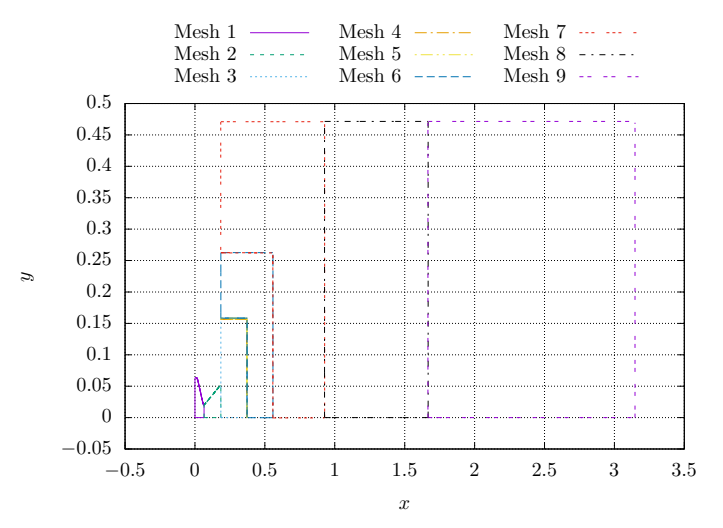


Fig. 6 Not to scale mesh configuration.

WENO-type weights to add more weight to lower-order stencils

$$\omega = \exp\left(-\|\beta\|^p/\epsilon\right),\tag{28}$$

with p = 1 and $\epsilon = 10^{-8}$.

For the verification, we show the absolute difference of the total temperature in Fig. 7 for the $\Delta x = r_{th}/160$ mesh. Despite the total temperature not being constant, we can see different regions in the flow. This happens because the total temperature of the atmosphere and chamber are different. At the symmetry line, we can see a rise in total temperature because of the interaction of shock waves and the Mach disk. Since the flow becomes supersonic after the nozzle throat, we can draw conclusions over the convergent part. One can see that the inflow, symmetry, and wall boundary treatments do not present a significant rise in the total temperature. One should expect a noticeable temperature rise due to friction in hypersonic flows [1]. In addition to the Couette flow accuracy test, we believe the nozzle flow is verified.

The rise in total temperature difference near the nozzle exit is due to recirculation, as shown in Fig. 8 for the $\Delta x = r_{th}/160$ mesh. Although valid, the wall pressure does not agrees with the experimental data of [7]. We remark that our results agree with other numerical and experimental data [2–6, 30, 31]. The subsonic entrainment region near the nozzle exit is the result of a free-shock separation. This is a known phenomenon that occurs in low nozzle pressure ratios (NPR) and is studied for, e.g., thrust-optimized parabolic nozzle contours [3].

We show the Mach number color map in Fig. 9 for the $\Delta x = r_{th}/160$ mesh. One can see the subsonic entrainment region near the nozzle exit, the oblique shock, triple point, Mach disk, and the diamond-shaped pattern of nozzle

Verification and validation of high-resolution inviscid and viscous conical nozzle flows

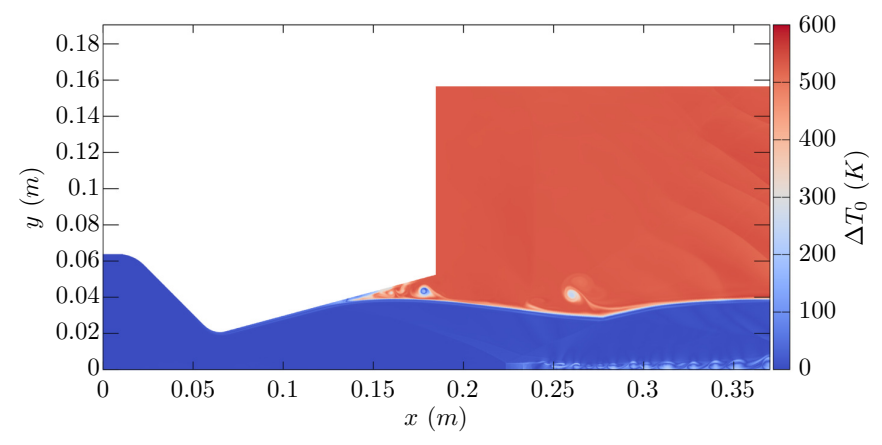


Fig. 7 Absolute difference of the total temperature for the viscous flow and $\Delta_x = r_{th}/160$ mesh.

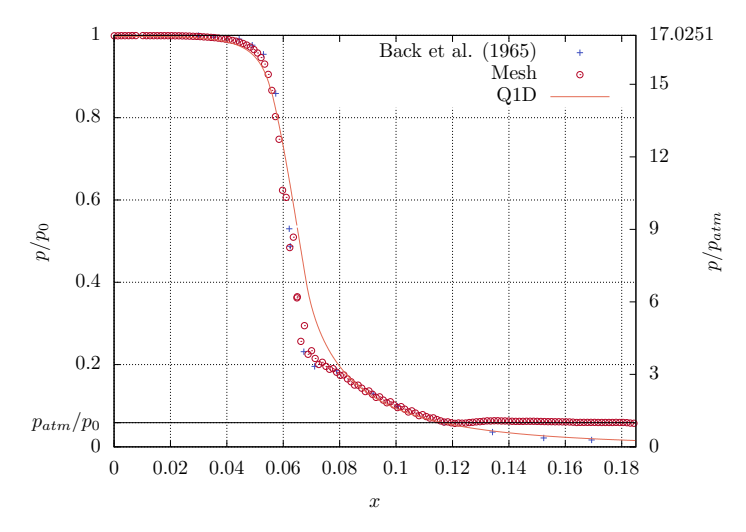


Fig. 8 Nozzle wall pressures for the viscous flow and $\Delta x = r_{th}/160$ mesh.

plumes. The flow will not reach a steady state because of the presence of vortices in different regions of the flow, and we are solving the Navier–Stokes equations without any type of averaging. In other words, the Mach disk will slowly move, and the plume contour will also change. We also show details of the subsonic entrainment in Fig. 10. We mark the velocity vectors with arrowheads to show the recirculation and flow pattern in the region. As stated in [32], the separation will occur in overexpanded jets, and a good grid resolution is required to predict the separation and turbulence structures. Also, the authors remark that downstream shock-cell formation can be affected. We remark

Verification and validation of high-resolution inviscid and viscous conical nozzle flow

that our numerical methods can capture elaborated structures and phenomena. However, the observed separation and related phenomena are regarded as preliminary results. More experimental data are required to validate the separation position and turbulence structures.

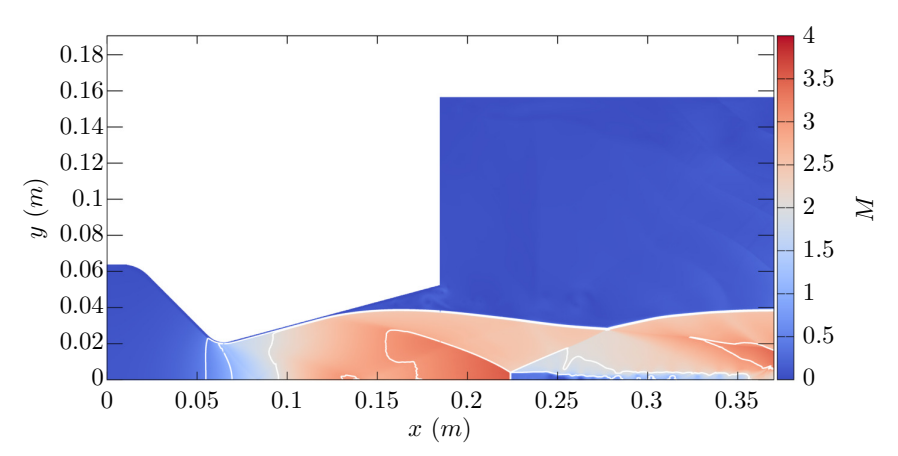


Fig. 9 Mach number color map for the viscous flow and $\Delta_x = r_{th}/160$ mesh.

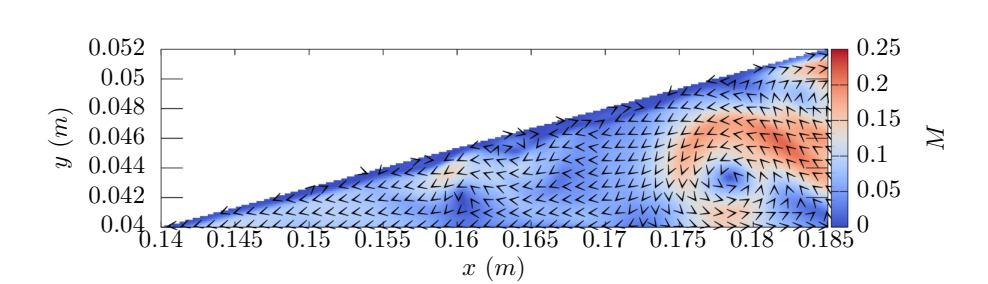


Fig. 10 Mach number color map and details of the subsonic entrainment region for the $\Delta_x = r_{th}/160$ mesh.

5 Concluding remarks

As in other challenging engineering applications, the nozzle flow has elaborated flow structures and phenomena. Even in a 2D numerical analysis, one should perform a multiphysics analysis to capture the phenomena. It is not rare to find a lack of agreement between numerical results and experimental data. Either because of the employed methods or lack of information for the boundary

Verification and validation of high-resolution inviscid and viscous conical nozzle flows

treatment. This is a typical situation as the numerical methods are being improved, for instance, the WENO schemes. We perceived the effort towards DNS and tested our methodology in a nozzle flow without turbulence models.

We checked the accuracy, verified and validated our methods for inviscid and viscous flows. The former with a vortex flow and the latter with a Couette flow. We solved nozzle flows for the $45\,^\circ-15\,^\circ$ conical profile of [7]. For the inviscid flow, we captured an oblique shock, and the numerical results agree with the experimental data. For the viscous flow, we captured more flow structures and elaborated phenomena. The flow is overexpanded, and we can see a reentrance region with recirculation and entrainment. The entrainment region is a result of a free-shock separation. We can see the oblique shock and a Mach disk forming near the nozzle exit. We can also see the diamond-shaped pattern of nozzle flows. Although the wall pressure does not agrees with the experimental data, we believe the numerical solution is valid. The inviscid flows show that the pressure is lower than the atmospheric at the reentrance region. Therefore, we expect the air outside the nozzle would reenter it.

Declarations

- The authors have no relevant financial or non-financial interests to disclose.
- The authors have no competing interests to declare that are relevant to the content of this article.
- All authors certify that they have no affiliations with or involvement in any organization or entity with any financial interest or non-financial interest in the subject matter or materials discussed in this manuscript.

References

- [1] Anderson, J.D.: Modern Compressible Flow, 3rd edn. McGraw-Hill, New York (2003)
- [2] Verma, S.B., Haidn, O.: Cold gas testing of thrust-optimized parabolic nozzle in a high-altitude test facility. Journal of Propulsion and Power **27**(6), 1238–1246 (2011). https://doi.org/10.2514/1.B34320
- [3] Baars, W.J., Tinney, C.E., Ruf, J.H., Brown, A.M., McDaniels, D.M.: Wall pressure unsteadiness and side loads in overexpanded rocket nozzles. AIAA Journal **50**(1), 61–73 (2012). https://doi.org/10.2514/1.J051075
- [4] Yaravintelimath, A., B.N., R., nigo, J.A.M.: Numerical prediction of nozzle flow separation: Issue of turbulence modeling. Aerospace Science and Technology **50**, 31–43 (2016). https://doi.org/10.1016/j.ast.2015.12.016
- [5] Martelli, E., Saccoccio, L., Ciottoli, P.P., Tinney, C.E., Baars, W.J.,

Verification and validation of high-resolution inviscid and viscous conical nozzle flow

Bernardini, M.: Flow dynamics and wall-pressure signatures in a high-

Revnolds-number overexpanded nozzle with free shock separation. Jour-

nal of Fluid Mechanics 895, 29 (2020). https://doi.org/10.1017/jfm.2020.

loads reduction in a sub-scale dual-bell rocket nozzle. Flow, Turbu-

lence and Combustion 107, 551–574 (2021). https://doi.org/10.1007/

dicted flows through conical supersonic nozzles, with emphasis on the

increasingly higher order of accuracy. Journal of Computational Physics

resolution ILW outflow boundary treatment for the Navier-Stokes

equations. Computers & Fluids **242**, 105506 (2022). https://doi.org/10.

WENO schemes for compressible Euler equations. Journal of Computa-

tional Physics **231**(5), 2245–2258 (2012). https://doi.org/10.1016/j.jcp.

Journal of Computational Physics 313, 726–753 (2016). https://doi.org/

weighted essentially non-oscillatory schemes for hyperbolic conservation

laws, pp. 325–432. Springer, Berlin, Heidelberg (1998). https://doi.org/

procedure for numerical boundary conditions of convection-diffusion

cedure for hyperbolic conservation laws with changing wind direction on

the boundary. Journal of Computational Physics, 109940 (2020). https:

[6] Cimini, M., Martelli, E., Bernardini, M.: Numerical analysis of side-

[7] Back, L.H., Massier, P.F., Gier, H.L.: Comparison of measured and pre-

[8] Zhu, J., Shu, C.-W.: A new type of multi-resolution WENO schemes with

[9] Araki, L.K., de R. Borges, R.B., da Silva, N.D.P., Shu, C.-W.: High-

[10] Zhang, X., Shu, C.-W.: Positivity-preserving high order finite difference

[11] Acker, F., Borges, R.B.R., Costa, B.: An improved WENO-Z scheme.

[12] Shu, C.-W.: In: Quarteroni, A. (ed.) Essentially non-oscillatory and

[13] Lu, J., Fang, J., Tan, S., Shu, C.-W., Zhang, M.: Inverse Lax-Wendroff

10.1007/BFb0096355. http://dx.doi.org/10.1007/BFb0096355

, 659–683 (2018). https://doi.org/10.1016/j.jcp.2018.09.003

transonic region. AIAA Journal **3**(9), 1606–1614 (1965)

s10494-021-00243-4

1016/j.compfluid.2022.105506

10.1016/j.jcp.2016.01.038

//doi.org/10.1016/j.jcp.2016.04.059

//doi.org/10.1016/j.jcp.2020.109940

2011.11.020

- [14] Lu, J., Shu, C.-W., Tan, S., Zhang, M.: An inverse Lax-Wendroff pro-

Methods in Engineering (2021)

s10915-006-9078-8

[16] Ning, W., He, L.: Some modeling issues on trailing-edge vortex shedding. AIAA Journal 39(5), 787–793 (2001). https://doi.org/10.2514/2.1411
[17] Sieverding, C., Manna, M.: A review on turbine trailing edge flow. International Journal of Turbomachinery, Propulsion and Power 5(2) (2020). https://doi.org/10.3390/ijtpp5020010

Verification and validation of high-resolution inviscid and viscous conical nozzle flows

resolution viscous terms discretization and ILW solid wall boundary

treatment for the Navier-Stokes equations. Archives of Computational

[15] Borges, R.B.de R., da Silva, N.D.P., Gomes, F.A.A., Shu, C.-W.: High-

[18] Verma, S.B., Hadjadj, A., Haidn, O.: Origin of side-loads in a subscale truncated ideal contour nozzle. Aerospace Science and Technology 71, 725–732 (2017). https://doi.org/10.1016/j.ast.2017.10.014

[19] Kumar, S., Ghosh, S.: Application of bandwidth-optimized WENO

, 69–102 (2022). https://doi.org/10.1007/s00193-021-01052-4

schemes to DNS of shock-turbulence interaction problems. Shock Waves

[20] Tan, S., Wang, C., Shu, C.-W., Ning, J.: Efficient implementation of high order inverse Lax—Wendroff boundary treatment for conservation laws. Journal of Computational Physics 231, 2510–2527 (2012). https://doi.org/10.1016/j.jcp.2011.11.037
[21] Borges, R.B.d.R., da Silva, N.D.P., Gomes, F.A.A., Shu, C.-W., Tan, S.:

A sequel of inverse Lax-Wendroff high order wall boundary treatment

Scientific Computing 28(2), 307–318 (2006). https://doi.org/10.1007/

- for conservation laws. Archives of Computational Methods in Engineering (2021). https://doi.org/10.1007/s11831-020-09454-w

 [22] Gottlieb, S., Gottlieb, D., Shu, C.-W.: Recovering high-order accuracy in WENO computations of steady-state hyperbolic systems. Journal of
- [23] da Silva, N.D.P., Marchi, C.H., Araki, L.K., de Rezende Borges, R.B., Bertoldo, G., Shu, C.-W.: Completed repeated Richardson extrapolation for compressible fluid flows. Applied Mathematical Modelling 77, 724–737 (2020). https://doi.org/10.1016/j.apm.2019.07.024
- [24] Rao, G.V.R.: Exhaust nozzle contour for optimum thrust. Journal of Jet Propulsion **28**(6), 377–382 (1958). https://doi.org/10.2514/8.7324
- [25] Spinelli, A., Cammi, G., Gallarini, S., Zocca, M., Cozzi, F., Gaetani, P., Dossena, V., Guardone, A.: Experimental evidence of non-ideal compressible effects in expanding flow of a high molecular complexity vapor. Experiments in Fluids 59(8) (2018). https://doi.org/10.1007/

[26] Sun, D., Luo, T., Feng, Q.: New contour design method for rocket nozzle of large area ratio. International Journal of Aerospace Engineering (2019).

https://doi.org/10.1155/2019/4926413

s00348-018-2578-0

[27] SERRA, R.C.O.: Determination of internal gas flows by a transient numerical technique. AIAA Journal 10(5), 603-611 (1972). https://doi. org/10.2514/3.50163

[28] Bell, I.H., Wronski, J., Quoilin, S., Lemort, V.: Pure and pseudo-pure fluid thermophysical property evaluation and the open-source thermophysical

[29] Kurita, N., Jourdaine, N.H., Tsuboi, N., Ozawa, K., Hayashi, K.A.,

//doi.org/10.2514/1.B35971

property library CoolProp. Industrial & Engineering Chemistry Research (6), 2498–2508 (2014). https://doi.org/10.1021/ie4033999

aiaa.org/doi/abs/10.2514/6.2020-0688

Kojima, T.: Three-Dimensional Numerical Simulation on Hydrogen/Air Rotating Detonation Engine with Aerospike Nozzle: Effects of Noz-

Verification and validation of high-resolution inviscid and viscous conical nozzle flow

zle Geometries, (2020). https://doi.org/10.2514/6.2020-0688. https://arc.

[30] Kharati-Koopaee, M., Khaef, I.: Numerical study of wall cooling effects on transition between shock structures in a rocket propulsion nozzle. Proceedings of the Institution of Mechanical Engineers, Part G: Journal of Aerospace Engineering **229**(1), 172–184 (2015). https://doi.org/10.1177/

[31] Stark, R., Génin, C.: Optimization of a rocket nozzle side load reduction device. Journal of Propulsion and Power 32(6), 1395–1402 (2016). https: [32] Liu, J., Khine, Y.Y.: Nozzle Boundary-Layer Separation Near the Nozzle Exit in Highly Overexpanded Jets, (2020). https://doi.org/10.2514/6. 2020-2561. https://arc.aiaa.org/doi/abs/10.2514/6.2020-2561